

VISTA3D: Versatile Imaging Segmentation and Annotation model for 3D Computed Tomography

Yufan He¹, Pengfei Guo¹, Yucheng Tang¹, Andriy Myronenko¹, Vishwesh Nath¹, Ziyue Xu¹, Dong Yang¹, Can Zhao¹, Benjamin Simon^{3,4}, Mason Belue², Stephanie Harmon³, Baris Turkbey³, Daguang Xu¹, Wenqi Li¹

¹ NVIDIA

² University of Arkansas for Medical Sciences

³National Institutes of Health

⁴ University of Oxford

Abstract. Medical image segmentation is a core component of precision medicine, and 3D computed tomography (CT) is one of the most important imaging techniques. A highly accurate and clinically applicable segmentation foundation model will greatly facilitate clinicians and researchers using CT images. Although existing foundation models have attracted great interest, none are adequate for 3D CT, either because they lack accurate automatic segmentation for large cohort analysis or the ability to segment novel classes. An ideal segmentation solution should possess two features: accurate out-of-the-box performance covering major organ classes, and effective adaptation or zero-shot ability to novel structures. To achieve this goal, we introduce **Versatile Imaging Segmentation and Annotation model (VISTA3D)**. VISTA3D is trained systematically on 11454 volumes and provides accurate out-of-the-box segmentation for 127 common types of human anatomical structures and various lesions. Additionally, VISTA3D supports 3D interactive segmentation, allowing convenient editing of automatic results and achieving state-of-the-art annotation results on unseen classes. The novel model design and training recipe represent a promising step toward developing a versatile medical image foundation model and will serve as a valuable foundation for CT image analysis. Code and model weights are available at <https://github.com/Project-MONAI/VISTA>

1 Introduction

Computed tomography (CT) is a widely used imaging modality for creating cross-sectional volumetric images within various body regions. As a major anatomic imaging modality, it reveals detailed morphological information of body structures and abnormalities. The CT image segmentation can facilitate diagnosis, treatment planning, and disease monitoring. In clinical practice, manual segmentation is time-consuming and tedious, thus developing better automatic models has been one of the most active research topics. A typical direction is enhancing network architecture and tailoring training recipes for specific tasks [32,17,44,20]. However, for each task, curating a specific set of training data and labels is often required.

Recently, large language models [45,2,47] have shown strong generalizability on various tasks and are considered the foundation models. The idea of a “promptable” system has been proposed to achieve a flexible model that can solve different tasks out-of-the-box.

For image segmentation, SAM has gained great interest and achieved impressive zero-shot performance. In the medical domain, recent works [28,49,12,50] hence adapted SAM to medical imaging modalities via model fine-tuning and optimized prompt generation and propagation. These SAM-based methods demonstrate promising results in 2D and can leverage interactive user input. For 3D medical images, such prompt (e.g. point) binding to every class, every slice, and every scan, often requires substantial effort, making it infeasible for large cohort data analysis.

Another category of works approaches the challenge from a different perspective: unlike natural images where there could be an unlimited number of object classes, the clinically relevant human anatomies revealed by CT can be considered a finite set with a limited number of classes (such as liver, pancreas), thus training an automated segmentation model can sufficiently cover most of the regions of interests and common use cases [7,26,22,51,48]. However, in practice, due to data scarcity (e.g. rare pathologies), lacking zero-shot capability becomes a significant system limitation in building a robust and versatile segmentation model.

Recent works exploring in-context learning for medical image segmentation [9,41] can segment any class guided by example image or text. This seems like an optimal case because it does not require model finetuning. However, the performance of such methods is lacking compared to the dataset-specific supervised models (e.g. nnUnet [20]).

We envision that a foundation model for 3D CT image segmentation should have the following essential capabilities: 1) Accurate automatic segmentation for clinically relevant common organs or structures; 2) Ability to interact with human experts, allowing for effective refinements of existing segmentation results; 3) Zero-shot capabilities, either allow the user to interactively annotate unseen classes or use in-context learning via text or example guidances. The model should operate in 3D since 2D slice-by-slice methods are too time-consuming and may not fully leverage 3D visual contexts; and 4) Few shot/transfer learning abilities that allow users to quickly adapt the model to perform segmentation on new classes.

Given our definition of the foundation model for CT segmentation above, the clinical segmentation workflow could be:

1. For common classes that have enough labeled data for model training, e.g. liver, the foundation model should perform state-of-the-art out-of-the-box automatic segmentation.
2. If segmentation is inaccurate, users can carry out a few rounds of refinements by clicking.
3. The model should achieve accurate zero-shot segmentation with minimal annotation effort.
4. With a few annotated examples, users can finetune the model and continue the steps.

In order to support this workflow, we developed novel training methods and model architecture. In this paper, we introduce the VISTA3D model:

1. High-accuracy and generalizability of promptable 3D automatic and interactive segmentation for supported 127 classes.
2. State-of-the-art zero-shot performance of 3D interactive segmentation for unseen classes, with much less annotation efforts.

3. We curated a large CT dataset with 11454 scans, paired it with partial manual labels, pseudo labels, and supervoxels, and proposed a novel model and recipe to achieve state-of-the-art performances.

2 Related Work

Dataset-specific supervised training. Many existing 3D medical imaging segmentation methods [32,17,44,20] are proposed to train dedicated models for a specific dataset. nnU-Net [20] functions as a framework that can automatically adapt to different datasets. This adaptation occurs seamlessly, mitigating the need for manual intervention or specialized expertise, which expedites the medical imaging segmentation models. Recently, Auto3DSeg¹ [33,34,35] presents a holistic approach to tackling the challenge of large-scale 3D medical image segmentation. It harnesses cutting-edge advancements in MONAI [10] and GPU technology to streamline the creation and implementation of algorithms, offering top-notch performance suitable for both novices and seasoned researchers. Although auto-configuration solutions like nnUNet and Auto3DSeg have proven their effectiveness by winning several highly competitive MICCAI challenges, the resulting dedicated models are constrained to specific tasks and typically lack inherent zero-shot capabilities.

Foundational CT segmentation model. Foundation segmentation models aim to develop a single unified deep learning model capable of segmenting multiple anatomical structures/organs from whole-body CT scans, rather than training separate models for each organ. Totalsegmentator [7] is proposed for fully automatic segmentation of over 117 anatomical structures in CT images covering various organs, bones, muscles, and vessels. It represents a significant contribution to the biomedical imaging community, enabling researchers and clinicians to leverage accurate and comprehensive segmentation without requiring time-consuming manual efforts. The Universal Model [26] leverages text embeddings from the CLIP model to encode the anatomical relationships between organs and tumors, instead of using traditional one-hot encoding for labels. This CLIP-based label encoding allows the model to learn structured feature representations capturing the semantics of different anatomical structures and enables efficient multi-task learning in a unified architecture. Another direction explored the multi-organ segmentation is continual learning. Continual Segment [22] is a unified model capable of segmenting various organs by leveraging continual learning techniques to incrementally expand its segmentation capabilities without catastrophically forgetting previously learned structures. While those foundational CT segmentation models represent significant advancements in multi-organ segmentation for CT scans, the inability of zero-shot and interactive segmentation impedes their real-world applicability. In addition, explorations into in-context learning [41] and CrossBlock mechanism [9] have been conducted to adapt the trained segmentation model for novel segmentation tasks without additional training. However, typically, their performance falls short compared to models trained on the specific dataset.

Interactive medical image segmentation. The Segment Anything Model (SAM) has inspired and enabled various medical imaging applications through the adaptation and fine-tuning on domain-specific data [19]. MedSAM [28] is proposed to leverage the capabilities of SAM aims to bridge the gap of existing segmentation methods that are often tailored to specific modalities or disease types, lacking generalizability. SAM-Med3D [49]

¹ <https://monai.io/apps/auto3dseg>

adapts the network architecture of SAM for the 3D medical image domain, which requires far fewer user-provided prompts compared to the existing 2D SAM variant [12] but lacks the ability of automatic segmentation for known classes. The work closely related to ours is SegVol [14], a 3D foundation model designed for semantic and interactive segmentation of volumetric medical images based on user prompts. SegVol [14]’s performance relies on 3D bounding-box and text prompts, and there is still a performance gap in its automatic and point based segmentation. Annotation with 3D bounding boxes are hard and not intuitive for humans, especially for complicated structures like colon.

3 Method

3.1 Overview

We separate the segmentation tasks into **supported classes** and **zero-shot classes**. The supported classes are the classes that have enough training data with annotations with which we can train VISTA3D to perform automatic segmentation. We curated an index list for supported classes and trained the automatic head to accept the index as the prompt and output a binary segmentation for the class. For zero-shot classes, the segmentation is only supported by VISTA3D interactive branch, which accepts user click points on 3D space. The interactive segmentation also works for supported classes. To train such a model, we curated a large dataset containing 11454 3D CT scans, generated pseudo labels from TotalSegmentator model [7] and supervoxels using SAM pre-trained weights [24]. A stage-by-stage training recipe is used to train interactive and automatic separately.

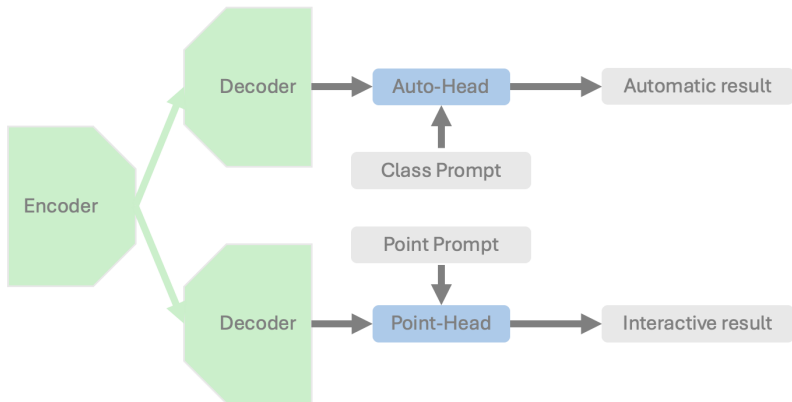


Fig. 1. The VISTA3D model contains two branches that share the same image encoder. The top auto-branch performs out-of-the-box automatic segmentation for 127 supported classes. The bottom interactive branch accepts user clicks and performs interactive segmentation on both supported classes and novel zero-shot classes.

3.2 Model

SAM’s [24] image encoder is a vision transformer (ViT) [25] with 16x16 patch embedding. For 3D images, ViT becomes extremely memory-demanding, since the token length (number of patches) is much longer compared to 2D images. On the other hand, 16x16 patch embedding inevitably loses spatial details. Computationally feasible adaptations of transformers to 3D images have been proposed [15,16], but the state-of-the-art results, as shown in the recent MICCAI 3D segmentation challenges, are still predominantly based on the convolutional architectures. Specifically, the SegResNet model, a U-net type architecture, has won BraTS 2023 [32], KiTS 2023 [35] and Seg.A 2023 [33] MICCAI 3D segmentation challenges. In VISTA3D, we use SegResNet [32] from MONAI [10], as a backbone CNN, and followed the best practices in medical image segmentation of patch based training (we used 128 cubic patch) and sliding window inference.

Automatic branch As shown in Fig 1, there are two branches: the automatic branch and the interactive branch. The SegResNet encoder is shared between two branches for learning image embedding. Each branch has its own decoder with a skip connection with the shared encoder. The Auto-head contains a post-mapping layer P which contains 2 convolutional blocks, a MLP layer M , and a learnable $N \times C$ class embedding E_c , where N represents N supported classes. The output feature F from the decoder and the following P is of size $C \times H \times W \times D$. If the user wants to segment class n (this single number n is the input prompt for the auto-head), the corresponding class embedding $E_c[n]$ is used to map the feature into segmentation logits, $\text{sigmoid}(M(E_c[n]) \times F)$. We added this additional MLP layer M due to empirically better performance. By using prompts and binary segmentation, the partial label problem in our curated datasets is avoided, and the memory cost is reduced dramatically. We did not use text-prompts with CLIP-embedding because empirically it reduced the automatic performance since the embedding is frozen, and currently no work [14,26] that used CLIP embedding in medical imaging is able to generate competitive zero-shot or open vocabulary segmentation by simply providing the "text-name" of the novel class.

Interactive branch For the interactive branch, the click points’ 3D coordinates and their labels (positive or negative) are accepted as prompts for the point head. The point head is based on the SAM’s [24] point prompt encoder, where the feature map performs cross-attention with point embedding. We made several changes to satisfy the needs for 3D medical images: 1) To keep the high-resolution details, the point head input feature is in original image resolution. We added a 3D feature downsample convolutional layer within the point head to do a 2x downsample in each axis to save memory, and all the related operations including point embedding are changed to 3D. The downsampled feature and the point embedding will go through cross-attention transformers and then upsampled by 3D convolutions. 2) For some classes that have ambiguity, e.g. pancreas/pancreas tumor and colon/colon tumor, single point click cannot achieve satisfactory results for the tumor due to unclear tumor boundary and ambiguity. We were not able to reproduce SAM’s strategy of using multi-masking and confidence predictor, which may due to limited classes with ambiguity in our curated dataset. We ignore this problem for zero-shot classes since it only affects single-click scenario, and we expect optimal performance to be achieved by more than a single click for zero-shot segmentation. For supported class, we expect a single click to work well and this ambiguity becomes a problem. Since the user will know the class for supported classes, we added a special embedding for the

click point based on specific classes like colon/pancreas tumor to distinguish ambiguous classes. 3) Another challenge is that interactive branch needs to handle both supported classes and unseen classes (zero-shot), while there might be a conflict between these two tasks. Segmenting supported class with high accuracy will require the model to remember specific features about the class, for example, to overfit to the liver’s intensity, shape and position, such that 1-click can segment the whole liver. However, organ specific tuning could hurt zero-shot generalizability. We mitigate this problem by requiring user to explicitly separate these two tasks for the model, which will concatenate a zero-shot embedding or a supported-class embedding to the point embedding.

Interactive refinement over automatic results As can be seen in Fig. 1, the two branch outputs are independent from each other. The use case by combining the results is to interactively correct the automatic segmentation results. As illustrated in FocalClick [11], the interactive refinement over existing masks could destroy the correct part. We observe this behavior when simply combining the interactive results and the automatic results. We used the local refinement idea from FocalClick and proposed the following merging algorithm Alg. 1. The core idea is to add or remove only the connected component region that contains the point click to avoid unexpected modification.

Algorithm 1 Interactive refinement based on the automatic results

Require: I positive and J negative clicks P_p^i and P_n^j , automatic and interactive output M_a and M_p

Ensure: $size(M_a) = size(M_p)$

Denote "get 3D connected components" as $CC(\cdot)$.

$\{M_{add}^n\}_N \leftarrow CC((M_p - M_a) > 0)$ ▷ N added connected components

$\{M_{rm}^k\}_K \leftarrow CC((M_a - M_p) > 0)$ ▷ K removed connected components

if $\exists_{i=1, \dots, I} P_p^i \in M_a$ **then** $M_{add}^n = M_{add}^n \cup CC(M_p)$

end if ▷ If positive points in M_a , add M_p into addition candidates.

$M_{final_rm}, M_{final_add} \leftarrow \{\}, \{\}$

for $n = 1$ to N **do**

if $\exists_{i=1, \dots, I} P_p^i \in M_{add}^n$ **then** $M_{final_add} = M_{final_add} \cup M_{add}^n$

end if

end for

for $k = 1$ to K **do**

if $\exists_{j=1, \dots, J} P_n^j \in M_{rm}^k$ **then** $M_{final_rm} = M_{final_rm} \cup M_{rm}^k$

end if

end for

return $M_a + M_{final_add} - M_{final_rm}$

3.3 Data

We curated a collection of 11454 CT volumetric images obtained from in-house and publicly available data sources [37,38,5,6,21,3,36,7,42,18,40,43,8,4,23,39,46] with a wide range of acquisition protocols and subject conditions. Among these, five of them are without labels, and the rest have various voxel-wise annotation regions of interest, including anatomical

structures and lesions. The spatial resolutions are ranged from $0.45 \times 0.45 \times 0.45$ to $1.50 \times 1.50 \times 7.50$ (median: $0.88 \times 0.88 \times 1.50$) mm^3 . Each data source is randomly split into 64% training, 16% validation, and 20% test sets. We generated pseudo-labels of 117 classes using TotalSegmentator [7] and supervoxels for every scan. The unreliable pseudo-labels are removed by post-processing.

Supervoxel generation The vast majority of SAM’s zero-shot capabilities come from this large-scale supervised training on its 11 million diverse and fully annotated images [24]. Those annotations helped SAM learn how humans perceive an object, and become the image segmentation foundation model. However, the manual labels or pseudo-labels in 3D CT can only cover around one or two hundred of classes. We empirically found that this level of class diversity is not enough for the model to achieve SAM-like zero-shot ability in 3D. To solve this problem, most works decided to finetune SAM pretrained ViT checkpoint on 2D medical data to inherit this zero-shot ability, which inevitably limited the adaptability to 3D images. Here we propose a novel method to distill the image understanding ability from SAM by generating 3D supervoxels from 2D SAM feature maps. The algorithm is shown in Alg. 2. We perform a 3D supervoxel algorithm on the upsample SAM feature embedding, which is generated slice-by-slice in three views. An example of generated supervoxel results is shown in Fig. 2. We generate supervoxels for all 11454 CT scans and use them to train our interactive branch, and this gave VISTA3D zero-shot capabilities. SegVol [14] used a similar idea but the supervoxel generation is based on graph-cut, which is still on low-level image features. Instead, VISTA3D achieved better zero-shot performance through distilling knowledge from SAM.

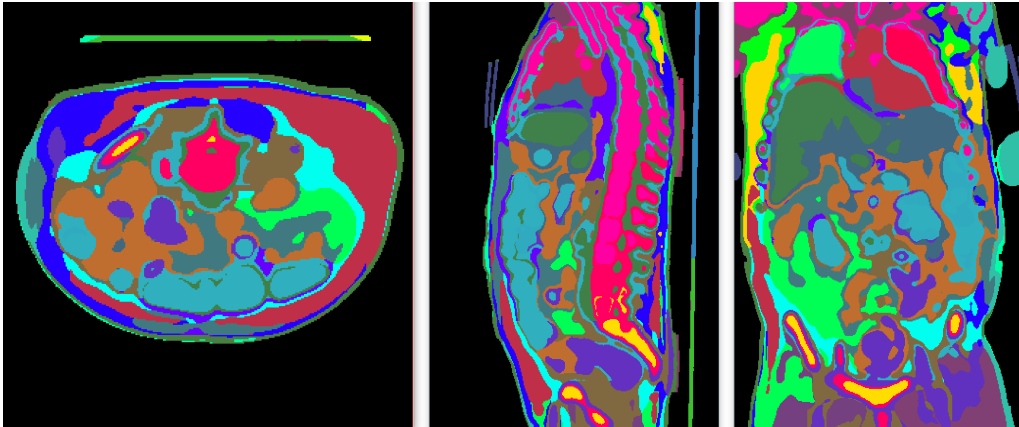


Fig. 2. Generated supervoxel from Alg. 2, showing examples in axial, sagittal, and coronal views. Different colours represent different supervoxels.

3.4 Recipe

The training has four stages to solve the class imbalance issues and complications between the automatic and interactive branches.

Algorithm 2 3D supervoxel generation from SAM

Require: SAM pretrained ViT-H model Φ , the image encoder Φ_E , the output scaling layer in the mask decoder Φ_s . \triangleright All SAM components related to prompts are removed

Ensure: Input 3D CT image V

$V \leftarrow \{x_1, x_2, \dots, x_A\}$ \triangleright Represent volume V as a stack of 2D axial slices

$V \leftarrow \{y_1, y_2, \dots, y_C\}$ \triangleright Represent volume V as a stack of 2D coronal slices

$V \leftarrow \{z_1, z_2, \dots, z_S\}$ \triangleright Represent volume V as a stack of 2D sagittal slices

$F_A, F_C, F_S \leftarrow \{\}, \{\}, \{\}$

for $i = 1$ to A **do**

$F_A = F_A \cup \Phi_s(\Phi_E(x_i))$ \triangleright Generate upsampled SAM feature for each slice at each axis.

end for

for $i = 1$ to C **do**

$F_C = F_C \cup \Phi_s(\Phi_E(y_i))$

end for

for $i = 1$ to S **do**

$F_S = F_S \cup \Phi_s(\Phi_E(z_i))$

end for

$F_{3D} \leftarrow F_A + F_C + F_S$ $\triangleright F_A, F_C, F_S$ are 3D tensors with the same size

return $SLIC(F_{3D}, n_{segments} = 100, sigma = 3)$ \triangleright We use SLIC [1] algorithm from skimage

Stage1-Interactive branch training: This is the first stage of VISTA3D training, and the goal is to train a strong image encoder that can extract good and generalizable features from 3D CT images, and enable the interactive branch to have good response to point clicks. In each iteration, the inputs contain randomly cropped 128 cubic image patches, corresponding manual labels, pseudo labels, and supervoxels. We use a point sampler to randomly sample point and its corresponding binary segmentation mask for training. The mask is generated by combining manual labels or pseudo labels with supervoxels or by supervoxels alone. The goal is to diversify the groundtruth and make the model responsive to all kinds of objects and boundaries. We also followed the SAM’s iterative training scheme and sampled new points from the false positive or negative regions from previous predictions to improve editing ability.

Stage2-Interactive branch finetuning: The data imbalance issue is severe in our curated dataset since some rare classes such as tumors are only presented in a limited number of images. Stage 1 have large number of training iterations and if we oversample under-represented classes during stage 1, those classes will soon overfit, moreover, overfit at different iterations for different classes. For simplicity, we disabled oversampling in stage 1 and under-represented classes were rarely sampled. In stage 2, we perform a quick finetuning with specific dataset oversampling to improve low-performing classes. Meanwhile, we removed the supervoxel and unlabeled dataset from this stage.

Stage3-Automatic branch training: The image encoder has been trained in the previous stages with all the 3D medical annotations and SAM-generated supervoxels. The training is based on binary segmentation without any class-specific information thus we can expect the encoder to generate more generalizable features. We freeze the image encoder to avoid changes to the interactive branch and train the auto branch decoder and head. The training is a common supervised training, but we random sample class prompts from 127 classes and use the corresponding binary masks as ground truth.

Stage4-Automatic branch finetuning: Similar to the interactive fine-tuning method, we employ a fine-tuning strategy on the automatic branch, focusing on improving the performance of under-represented classes within the datasets. A key difference lies in integrating the in-house Generative AI technique, leveraged to generate synthetic data containing anomalies such as tumors and lesions. Additional synthetic data allows us to enrich the diversity of the training data, thereby enhancing the robustness of the model. Following the generation of synthetic data, we uniformly sample data across all datasets to ensure equitable representation during the final training phase, facilitating the optimization of the final model across various classes and anomaly types.

4 Supported classes results

We first test the performance of the supported classes. For supported classes, we claim that the out-of-the-box performance of a foundational model should have state-of-the-art or comparable performances to the data-specific models, meanwhile, we claim VISTA3D interactive branch can correct error regions in automatic results. We test the VISTA3D’s out-of-the-box automatic segmentation results (VISTA3D auto), single positive click interactive results (VISTA3D point), and the corrected automatic results with single click points (VISTA3D auto + point) with Alg. 1. Note that VISTA3D is a patch-based method using sliding window inference, thus a click point will only affect the 128 cubic patch that includes the point. The evaluation with a single point means 1 click for each patch.

Table 1. Average dice score of supported classes of the test split in each dataset. TotalSegV2 results are biased towards nnUNet and TotalSegmentator (the groundtruth is generated by the pretrained TotalSegmentator model, which uses nnUNet architecture, and the training data may include our test split). The Bone Lesion is a private dataset of 237 whole-body CT scans.

	Auto3dSeg	nnUNet	TotalSegmentator	VISTA3D auto	VISTA3D point	VISTA3D auto+point
MSD03 Hepatic tumor [3]	0.616	0.617	-	0.588	0.701	0.687
MSD06 Lung tumor [3]	0.562	0.554	-	0.613	0.682	0.719
MSD07 Pancreatic tumor [3]	0.485	0.488	-	0.324	0.603	0.638
MSD08 Hepatic tumor [3]	0.683	0.659	-	0.682	0.733	0.757
MSD09 Spleen [3]	0.965	0.967	0.966	0.952	0.938	0.954
MSD10 Colon tumor [3]	0.475	0.473	-	0.439	0.609	0.633
Airway [43]	0.896	0.899	-	0.852	0.819	0.867
Bone Lesion	0.343	0.396	-	0.491	0.536	0.585
BTCV-Abdomen [37]	0.807	0.825	0.846	0.849	0.815	0.859
BTCV-Cervix [38]	0.598	0.640	0.611	0.672	0.736	0.775
VerSe [40]	0.786	0.828	0.832	0.825	0.896	0.906
AbdomenCT-1K [5]	0.934	0.939	0.921	0.935	0.903	0.940
AMOS22 [21]	0.854	0.854	0.824	0.841	0.785	0.856
TotalSegV2 [7]	0.882	*0.906	*0.942	0.893	0.884	0.918
Average	0.706	0.718	-	0.711	0.760	0.792

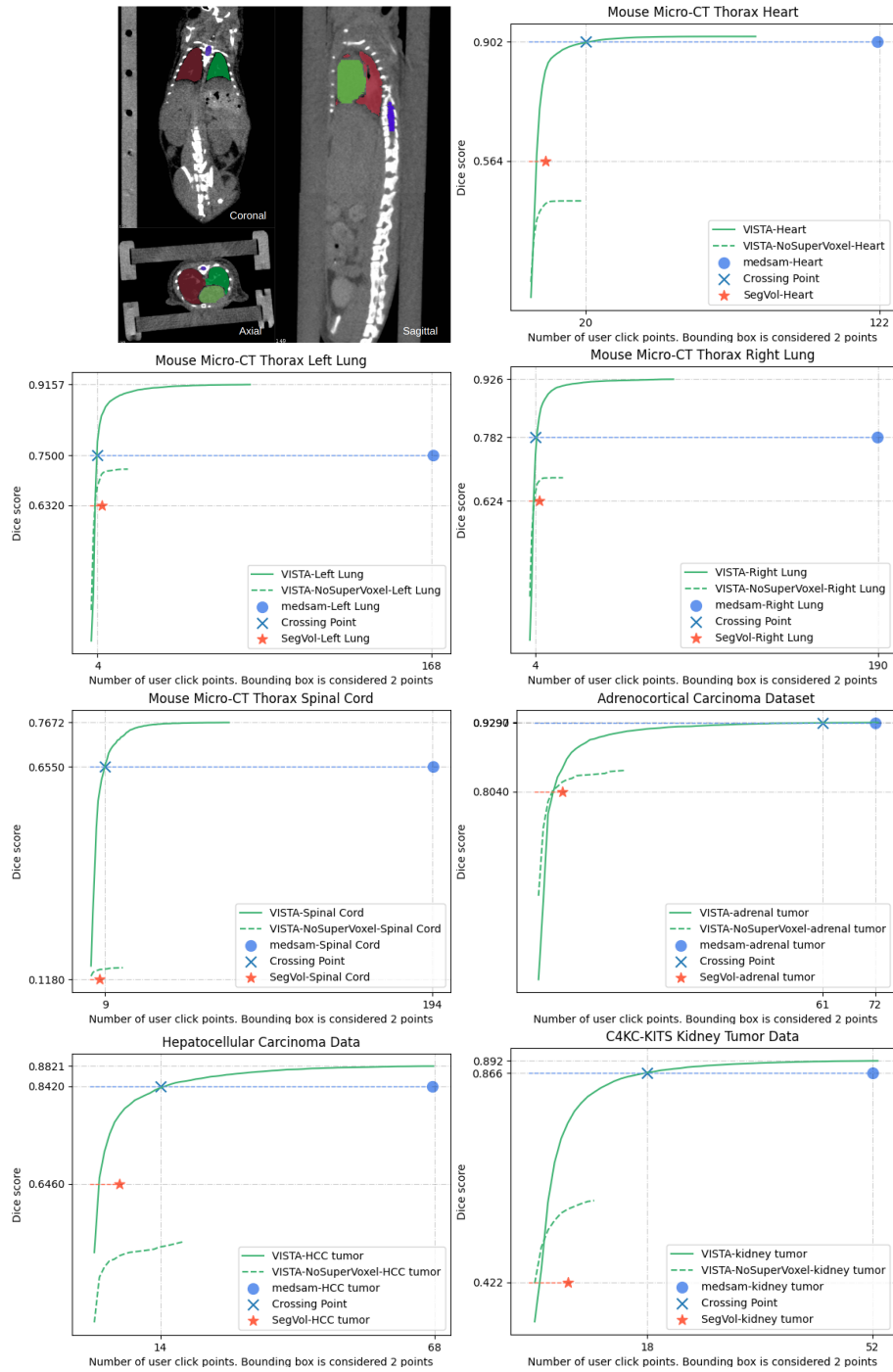


Fig. 3. The three-view mouse micro-CT example (first image). The rest are zero-shot dice scores. X-axis is the number of click points. Y-axis is the average dice score over the whole dataset.

5 Zero-shot results

In this section, we test the zero-shot ability of VISTA3D. We compare with MedSAM [28] and SegVol [14] as they showed the best interactive performances in 2D and 3D separately. For the MedSAM baseline, we adopt the 3D inference pipeline via a series of 2D slices as described in [28]. For segmentation targets that are larger than 10 voxels, tight bounding boxes for each slice were generated to simulate user-provided prompts. Each bounding box is considered the same annotation effort as two-point prompts in our evaluations. For the SegVol baseline, the default settings [14] are evaluated using a positive point with three pairs of positive and negative points (7 points in total), as well as the zoom-out-zoom-in inference strategy. For VISTA3D, We mimic user annotations to perform iterative point clicks. The first point is sampled at the foreground center, then the next point will be randomly sampled from the largest connected false positive or false negative region, which has a larger area size. We evaluate the performance of 4 novel external datasets. 1) the murine dataset [29] includes 140 scans with 4 annotated mouse organs: heart, left lung, right lung, and spinal cord. The CT scanning protocol and organ shapes are quite different to humans as shown in Fig. 3. 2) the C4KC-KITS (kidney tumor, 210 scans) dataset [18], the Adrenocortical Carcinoma (adrenal tumor, 53 scans) dataset [30,13], the Hepatocellular Carcinoma (liver tumor, 105 scans) dataset [31,13]. The results are shown in Fig. 3. The results show the superior performance of VISTA3D in both accuracy and reduced annotation efforts. VISTA3D trained without supervoxel (VISTA-NoSupervoxel) is also shown in the figure, and the results showed the importance of supervoxel for the zero-shot ability.

6 Finetuning results

In this section, we perform transfer learning on novel datasets. We perform finetuning on the automatic branch under the setting of one-shot, five-shot, until the full training dataset. The dataset we use includes the Whole abdominal Organs Dataset (WORD) [27] and the micro-CT mouse dataset [29]. We compare with training from scratch methods (nnUNet and Auto3DSeg, default setting), and finetuning Totalsegmentator pretrained checkpoint with default nn-Unet pipeline. We use the data split from WORD [27] and our own split for the mouse dataset. The results are shown in Table 2. Compared with the baselines, VISTA3D showed much better performance with fewer training data but plateaued with more data. The results support our claim where users can annotate a few examples and finetune VISTA3D.

7 Conclusion

In this paper, we proposed a 3D CT foundation segmentation model, VISTA3D. It achieved accurate segmentation comparable with specialised models trained for each dataset, state-of-the-art zero-shot interactive segmentation, and strong transfer learning ability. The large-scale high quality training data, carefully designed model architecture and training recipe were vital for building the highly capable models. All the component of VISTA3D is designed to fulfill our proposed workflow, and we also utilize the best

Table 2. Finetuning performances.

Dataset	Finetune # of cases	Auto3DSeg	nmUNet	TotalSegmentator	VISTA3D
Micro-CT Mouse [29]	1	0.820	0.759	0.791	0.926
	5	0.923	0.922	0.924	0.935
	10	0.934	0.930	0.936	0.938
	20	0.947	0.942	0.944	0.944
	40	0.949	0.949	0.949	0.948
	89	0.949	0.949	0.951	0.951
WORD [27]	1	0.214	0.185	0.779	0.795
	5	0.611	0.562	0.823	0.839
	10	0.744	0.697	0.837	0.855
	20	0.806	0.793	0.855	0.862
	40	0.862	0.831	0.857	0.869
	100	0.873	0.874	0.875	0.875

practices in 3D medical image analysis (e.g. sliding-window, patches, 3D convolutions) to improve the results.

Limitations VISTA3D currently only supports CT image which is a major limitation. Another limitation comes from the supervoxel, which may not represent meaningful objects and tends to be local. Training with those masks introduced strong uncertainty and VISTA3D tends to be conservative and failed to segment large objects like whole-body.

The future work includes 1) improving user experience, e.g. inference speed, better point response, and more supported classes. 2) developing methods to better utilize or distill datasets and models from natural images. 3) extending the model to other modalities.

References

- Achanta, R., Shaji, A., Smith, K., Lucchi, A., Fua, P., Süsstrunk, S.: SLIC superpixels compared to state-of-the-art superpixel methods. *IEEE transactions on pattern analysis and machine intelligence* **34**(11), 2274–2282 (2012)
- Achiam, J., Adler, S., Agarwal, S., Ahmad, L., Akkaya, I., Aleman, F.L., Almeida, D., Altenschmidt, J., Altman, S., Anadkat, S., et al.: GPT-4 technical report. *arXiv preprint arXiv:2303.08774* (2023)
- et al., A.: The medical segmentation decathlon. *Nature communications* **13**(1), 4128 (2022)
- et al., H.: Artificial intelligence for the detection of COVID-19 pneumonia on chest CT using multinational datasets. *Nature communications* **11**(1), 4080 (2020)
- et al., M.: Abdomenct-1k: Is abdominal organ segmentation a solved problem? *IEEE Transactions on Pattern Analysis and Machine Intelligence* **44**(10), 6695–6714 (2022). <https://doi.org/10.1109/TPAMI.2021.3100536>
- et al., M.: Unleashing the strengths of unlabeled data in pan-cancer abdominal organ quantification: the flare22 challenge. *arXiv preprint arXiv:2308.05862* (2023)
- et al., W.: TotalSegmentator: Robust segmentation of 104 anatomic structures in CT images. *Radiology: Artificial Intelligence* **5**(5), e230024 (2023)
- Armato III, S., McLennan, G., Bidaut, L., McNitt-Gray, M., Meyer, C., Reeves, A., Zhao, B., Aberle, D., Henschke, C., Hoffman, E., et al.: Data from LIDC-IDRI [data set]. The Cancer Imaging Archive (2015). <https://doi.org/10.7937/K9/TCIA.2015.L09QL9SX>

9. Butoi, V.I., Ortiz, J.J.G., Ma, T., Sabuncu, M.R., Guttag, J., Dalca, A.V.: Universeg: Universal medical image segmentation. In: Proceedings of the IEEE/CVF International Conference on Computer Vision. pp. 21438–21451 (2023)
10. Cardoso, M.J., Li, W., Brown, R., Ma, N., Kerfoot, E., Wang, Y., Murrey, B., Myronenko, A., Zhao, C., Yang, D., et al.: Monai: An open-source framework for deep learning in healthcare. arXiv preprint arXiv:2211.02701 (2022)
11. Chen, X., Zhao, Z., Zhang, Y., Duan, M., Qi, D., Zhao, H.: Focalclick: Towards practical interactive image segmentation. In: Proceedings of the IEEE/CVF Conference on Computer Vision and Pattern Recognition. pp. 1300–1309 (2022)
12. Cheng, J., Ye, J., Deng, Z., Chen, J., Li, T., Wang, H., Su, Y., Huang, Z., Chen, J., Jiang, L., Sun, H., He, J., Zhang, S., Zhu, M., Qiao, Y.: SAM-Med2D (2023)
13. Clark, K., Vendt, B., Smith, K., Freymann, J., Kirby, J., Koppel, P., Moore, S., Phillips, S., Maffitt, D., Pringle, M., et al.: The cancer imaging archive (TCIA): maintaining and operating a public information repository. *Journal of digital imaging* **26**, 1045–1057 (2013)
14. Du, Y., Bai, F., Huang, T., Zhao, B.: Segvol: Universal and interactive volumetric medical image segmentation. arXiv preprint arXiv:2311.13385 (2023)
15. Hatamizadeh, A., Tang, Y., Nath, V., Yang, D., Myronenko, A., Landman, B., Roth, H.R., Xu, D.: Unetr: Transformers for 3D medical image segmentation. In: Proceedings of the IEEE/CVF winter conference on applications of computer vision. pp. 574–584 (2022)
16. He, Y., Nath, V., Yang, D., Tang, Y., Myronenko, A., Xu, D.: SwinUNETR-V2: Stronger swin transformers with stagewise convolutions for 3D medical image segmentation. In: MICCAI (2023)
17. He, Y., Yang, D., Roth, H., Zhao, C., Xu, D.: Dints: Differentiable neural network topology search for 3d medical image segmentation. In: Proceedings of the IEEE/CVF conference on computer vision and pattern recognition. pp. 5841–5850 (2021)
18. Heller, N., Sathianathen, N., Kalapara, A., Walczak, E., Moore, K., Kaluzniak, H., Rosenberg, J., Blake, P., Rengel, Z., Oestreich, M., et al.: Data from C4KC-KITS [data set]. *The Cancer Imaging Archive* **10** (2019). <https://doi.org/10.7937/TCIA.2019.IX49E8NX>
19. Huang, Y., Yang, X., Liu, L., Zhou, H., Chang, A., Zhou, X., Chen, R., Yu, J., Chen, J., Chen, C., et al.: Segment anything model for medical images? *Medical Image Analysis* **92**, 103061 (2024)
20. Isensee, F., Jaeger, P.F., Kohl, S.A., Petersen, J., Maier-Hein, K.H.: nnU-Net: a self-configuring method for deep learning-based biomedical image segmentation. *Nature Methods* **18**(2), 203–211 (2021)
21. Ji, Y., Bai, H., Yang, J., Ge, C., Zhu, Y., Zhang, R., Li, Z., Zhang, L., Ma, W., Wan, X., et al.: AMOS: A large-scale abdominal multi-organ benchmark for versatile medical image segmentation. arXiv preprint arXiv:2206.08023 (2022)
22. Ji, Z., Guo, D., Wang, P., Yan, K., Lu, L., Xu, M., Wang, Q., Ge, J., Gao, M., Ye, X., et al.: Continual segment: Towards a single, unified and non-forgetting continual segmentation model of 143 whole-body organs in ct scans. In: Proceedings of the IEEE/CVF International Conference on Computer Vision. pp. 21140–21151 (2023)
23. Johnson, C.D., Chen, M.H., Toledano, A.Y., Heiken, J.P., Dachman, A., Kuo, M.D., Menias, C.O., Siewert, B., Cheema, J.L., Obregon, R.G., et al.: Accuracy of CT colonography for detection of large adenomas and cancers. *New England Journal of Medicine* **359**(12), 1207–1217 (2008)
24. Kirillov, A., Mintun, E., Ravi, N., Mao, H., Rolland, C., Gustafson, L., Xiao, T., Whitehead, S., Berg, A.C., Lo, W.Y., et al.: Segment anything. In: Proceedings of the IEEE/CVF International Conference on Computer Vision. pp. 4015–4026 (2023)
25. Kolesnikov, A., Dosovitskiy, A., Weissenborn, D., Heigold, G., Uszkoreit, J., Beyer, L., Minderer, M., Dehghani, M., Houtsby, N., Gelly, S., Unterthiner, T., Zhai, X.: An image is worth 16x16 words: Transformers for image recognition at scale. In: ICLR (2021)

26. Liu, J., Zhang, Y., Chen, J.N., Xiao, J., Lu, Y., A Landman, B., Yuan, Y., Yuille, A., Tang, Y., Zhou, Z.: Clip-driven universal model for organ segmentation and tumor detection. In: Proceedings of the IEEE/CVF International Conference on Computer Vision. pp. 21152–21164 (2023)
27. Luo, X., Liao, W., Xiao, J., Chen, J., Song, T., Zhang, X., Li, K., Metaxas, D.N., Wang, G., Zhang, S.: Word: A large scale dataset, benchmark and clinical applicable study for abdominal organ segmentation from ct image. *Medical Image Analysis* **82**, 102642 (Nov 2022)
28. Ma, J., He, Y., Li, F., Han, L., You, C., Wang, B.: Segment anything in medical images. *Nature Communications* **15**, 1–9 (2024)
29. Malimban, J., Lathouwers, D., Qian, H., Verhaegen, F., Wiedemann, J., Brandenburg, S., Staring, M.: Deep learning-based segmentation of the thorax in mouse micro-ct scans. *Scientific reports* **12**(1), 1822 (2022)
30. Moawad, A., Ahmed, A., et al.: Voxel-level segmentation of pathologically-proven adrenocortical carcinoma with Ki-67 expression (Adrenal-ACC-Ki67-Seg)[data set]. *The Cancer Imaging Archive* (2023)
31. Morshid, A., Elsayes, K.M., Khalaf, A.M., Elmohr, M.M., Yu, J., Kaseb, A.O., Hassan, M., Mahvash, A., Wang, Z., Hazle, J.D., et al.: A machine learning model to predict hepatocellular carcinoma response to transcatheter arterial chemoembolization. *Radiology: Artificial Intelligence* **1**(5), e180021 (2019)
32. Myronenko, A.: 3D MRI brain tumor segmentation using autoencoder regularization. In: MICCAI Brainles. Brain Tumor Segmentation (BraTS) Challenge. pp. 311–320. Springer (2018)
33. Myronenko, A., Yang, D., He, Y., Xu, D.: Aorta segmentation from 3D CT in MICCAI SEG.A. 2023 challenge. In: MICCAI 2023. 3D Segmentation of the Aorta Challenge (2023)
34. Myronenko, A., Yang, D., He, Y., Xu, D.: Auto3DSeg for brain tumor segmentation from 3D MRI in BraTS 2023 challenge. In: MICCAI. Brain Tumor Segmentation (BraTS) Challenge. (2023)
35. Myronenko, A., Yang, D., He, Y., Xu, D.: Automated 3D segmentation of kidneys and tumors in MICCAI KiTS 2023 challenge. In: MICCAI 2023. International Challenge on Kidney and Kidney Tumor Segmentation. pp. 1–7. Springer (2023)
36. Rister, B., Yi, D., Shivakumar, K., Nobashi, T., Rubin, D.L.: CT-ORG, a new dataset for multiple organ segmentation in computed tomography. *Scientific Data* **7**(1), 381 (2020)
37. Roth, H., Farag, A., Turkbey, E., Lu, L., Liu, J., Summers, R.: Data from pancreas-CT (version 2)[data set]. *The Cancer Imaging Archive* (2016). <https://doi.org/10.7937/K9/TCIA.2016.tNB1kqBU>
38. Roth, H.R., Lu, L., Farag, A., Shin, H.C., Liu, J., Turkbey, E.B., Summers, R.M.: Deeporgan: Multi-level deep convolutional networks for automated pancreas segmentation. In: MICCAI. pp. 556–564. Springer (2015)
39. Saltz, J., Saltz, M., Prasanna, P., Moffitt, R., Hajagos, J., Bremer, E., Balsamo, J., Kurc, T.: Stony Brook university COVID-19 positive cases. *the cancer imaging archive* **4** (2021). <https://doi.org/10.7937/TCIA.BBAG-2923>
40. Sekuboyina, A., Husseini, M.E., Bayat, A., Löffler, M., Liebl, H., Li, H., Tetteh, G., Kukačka, J., Payer, C., Štern, D., et al.: Verse: A vertebrae labelling and segmentation benchmark for multi-detector CT images. *Medical image analysis* **73**, 102166 (2021)
41. Shen, L., Shang, F., Yang, Y., Huang, X., Xiang, S.: Segicl: A universal in-context learning framework for enhanced segmentation in medical imaging. *arXiv preprint arXiv:2403.16578* (2024)
42. Simpson, A.L., Peoples, J., Creasy, J.M., Fichtinger, G., Gangai, N., Keshavamurthy, K.N., Lasso, A., Shia, J., D’Angelica, M.I., Do, R.K.: Preoperative CT and survival data for patients undergoing resection of colorectal liver metastases. *Scientific Data* **11**(1), 172 (2024)

43. Støverud, K.H., Bouget, D., Pedersen, A., Leira, H.O., Langø, T., Hofstad, E.F.: AeroPath: An airway segmentation benchmark dataset with challenging pathology. arXiv preprint arXiv:2311.01138 (2023)
44. Tang, Y., Yang, D., Li, W., Roth, H.R., Landman, B., Xu, D., Nath, V., Hatamizadeh, A.: Self-supervised pre-training of swin transformers for 3D medical image analysis. In: Proceedings of the IEEE/CVF conference on computer vision and pattern recognition. pp. 20730–20740 (2022)
45. Team, G., Anil, R., Borgeaud, S., Wu, Y., Alayrac, J.B., Yu, J., Soricut, R., Schalkwyk, J., Dai, A.M., Hauth, A., et al.: Gemini: a family of highly capable multimodal models. arXiv preprint arXiv:2312.11805 (2023)
46. Team, N.L.S.T.R.: Reduced lung-cancer mortality with low-dose computed tomographic screening. *New England Journal of Medicine* **365**(5), 395–409 (2011)
47. Touvron, H., Martin, L., Stone, K., Albert, P., Almahairi, A., Babaei, Y., Bashlykov, N., Batra, S., Bhargava, P., Bhosale, S., et al.: Llama 2: Open foundation and fine-tuned chat models. arXiv preprint arXiv:2307.09288 (2023)
48. Ulrich, C., Isensee, F., Wald, T., Zenk, M., Baumgartner, M., Maier-Hein, K.H.: Multi-dataset approach to medical image segmentation: Multitalent. In: BVM Workshop. pp. 78–78. Springer (2024)
49. Wang, H., Guo, S., Ye, J., Deng, Z., Cheng, J., Li, T., Chen, J., Su, Y., Huang, Z., Shen, Y., Fu, B., Zhang, S., He, J., Qiao, Y.: Sam-med3d (2023)
50. Wu, J., Fu, R., Fang, H., Liu, Y., Wang, Z., Xu, Y., Jin, Y., Arbel, T.: Medical SAM adapter: Adapting segment anything model for medical image segmentation. arXiv preprint arXiv:2304.12620 (2023)
51. Zhao, Z., Zhang, Y., Wu, C., Zhang, X., Zhang, Y., Wang, Y., Xie, W.: One model to rule them all: Towards universal segmentation for medical images with text prompts. arXiv preprint arXiv:2312.17183 (2023)

VISTA3D: Versatile Imaging Segmentation and Annotation model for 3D Computed Tomography

— *Supplementary Material* —

Yufan He¹, Pengfei Guo¹, Yucheng Tang¹, Andriy Myronenko¹, Vishwesh Nath¹, Ziyue Xu¹, Dong Yang¹, Can Zhao¹, Benjamin Simon^{3,4}, Mason Belue², Stephanie Harmon³, Baris Turkbey³, Daguang Xu¹, Wenqi Li¹

¹ NVIDIA

² University of Arkansas for Medical Sciences

³ National Institutes of Health

⁴ University of Oxford

1 Dataset Details

Table 1 lists more details about our curated dataset. Fig. 1 shows the number of annotated voxels according to the corresponding task classes.

Global and local index for partial label Those datasets have the different number of classes and indexes (e.g. Pancreas in MSD07 has index 1 but 10 in TotalsegmentatorV2) in their manual labels. We curated a global index of 127 integers and mapped all the local indexes in each individual dataset to this global index. We also curated a **label set** list for each dataset, containing the class index that will be used within this dataset.

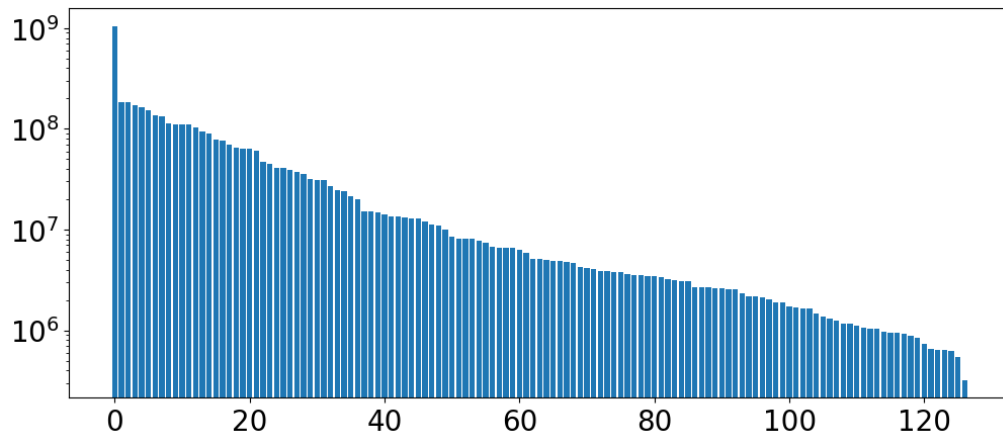


Fig. 1. Distribution of annotated voxels in the training set (X-axis: class index, Y-axis: number of annotated voxels per class).

Dataset ID	Type	# cases used
TCIA Pancreas CT [37]	Abdominal CT organs	80
AbdomenCT-1K [5]	Abdominal CT organs	1,050
AMOS22 [21]	Abdominal CT organs	300
MSD Task 3,6,7,8,9,10 [3]	Various lesions	945
CT-ORG [36]	Lung, bones, liver, kidneys, bladder	136
TotalSegmentator [7]	Many anatomic structures	1,228
CRML-CT [42]	Liver, colorectal liver metastases	197
VerSe [40]	Vertebral labelling	374
AeroPath [43]	Airways and lungs	27
Bone lesion (in-house)	bones	296
LIDC-IDRI [8]	Unannotated, lung cancer screening thoracic	470
COVID-19 [4]	Unannotated, chest	524
TCIA Colonography [23]	Unannotated, abdomen	1,440
StonyBrook COVID19 CT [39]	Unannotated, chest	1,274
NLST [46]	Unannotated, chest	3,113

Table 1. Summary of datasets used for model training.

2 Additional training details

2.1 Stage1-Interactive branch training

The algorithm is shown in Alg. 1. The point sampler S works as a data augementer, with 50% probability to sample points directly from y to get the point p and binary groundtruth mask y_{gt} as a training pair, while another 50% will be used with the following augmentations: a) random sample points from supervoxel and form a zero-shot training pair. b) random add or subtract a supervoxel mask that satisfies a certain size and position criterion to y , this is used to force the model to be able to edit supported class mask. Meanwhile, when the subtraction or addition size exceeds a certain limit, the generated training pair will also be used as zero-shot pairs with the zero-shot embedding. We use $max_{iter} = 5$ for the training.

2.2 Stage3-Automatic branch training

For each patch, we randomly sample the existing class indexes c from its manual label or pseudo label, and get the corresponding binary mask y_{gt} or y_{gt}^p . The algorithm is shown in Alg. 2. Unlike traditional segmentation models that do softmax on multichannel output, our automatic segmentation is based on promptable binary segmentation, thus prone to produce false positives. We mitigate this issue by sampling the background prompts from $label_set - y.unique()$ or $label_set - y^p.unique()$ and train the model to produce empty output when giving the prompt. So in each iteration, a 128 cubic image patch is the model input, and we sample a maximum of 32 class prompts using Alg. 2 and a maximum of 4 background prompts. All of those prompts are concatenated in the batch dimension.

3 Addition Results

We provide additional VISTA3D results in this section.

Algorithm 1 Interactive branch training

Require: VISTA interactive branch model Φ , image patch x , image manual label y , image pseudo label y_p , supervoxel y_s .

Ensure: At least one of y or y_p are not None

$S \leftarrow \text{point_sampler}(y, y_s)$ \triangleright Initialize point sampler based on manual label and supervoxel
 $S_p \leftarrow \text{point_sampler}(y_p, y_s)$

$p, y_{gt} \leftarrow S.\text{sample}()$ \triangleright Sample point prompts p and segmentation mask y_{gt}

$p^p, y_{gt}^p \leftarrow S.\text{sample}()$

for $i = 1$ to max_iter **do**

$\text{loss} \leftarrow \text{LossFunction}(\Phi(x, p), y_{gt})$

$\text{loss}_p \leftarrow \text{LossFunction}(\Phi(x, p^p), y_{gt}^p)$

 update Φ using $\text{loss} + \text{loss}_p$

$p = p \cup \text{Sample}(\Phi(x, p), y_{gt})$ \triangleright Sample 1 point each from false positive and negative region

$p^p = p^p \cup \text{Sample}(\Phi(x, p^p), y_{gt}^p)$

end for

Algorithm 2 Automatic branch training

Require: VISTA automatic branch model Φ_a with encoder frozen, image patch x , image manual label y , image pseudo label y_p .

Ensure: At least one of y or y_p are not None

$c, y_{gt} \leftarrow y.\text{unique}().\text{sample}()$ \triangleright Sample class prompts c and segmentation mask y_{gt}

$c^p, y_{gt}^p \leftarrow y_p.\text{unique}().\text{sample}()$

$\text{loss} \leftarrow \text{LossFunction}(\Phi_a(x, c), y_{gt})$

$\text{loss}_p \leftarrow \text{LossFunction}(\Phi_a(x, c^p), y_{gt}^p)$

update Φ_a using $\text{loss} + \text{loss}_p$

3.1 Qualitative Results

Visualizations of VISTA3D predictions are provided in this section.

Generalizability of the automatic segmentation We show the generalizability of VISTA3D automatic segmentation by testing on an in-house whole-body **monkey** CT, as shown in Fig. 2.

Correcting automatic segmentation with points We show an example of correcting automatic segmentation with points, as shown in Fig. 3.

Zero-shot interactive examples In Fig. 4, we show the iterative point clicks of a kidney tumor. From step 1 to step 3 we can see how the segmentation responds to the clicks. Fig. 5 shows the responses on other slices without clicks. This shows the click response in 3D. In Fig. 6, we show the interactive segmentation on a micro-CT mouse left lung. The baseline MedSAM [28] and SegVol [14] results are from their provided user interface and online hugging-face demo. We can see that MedSAM has a major weakness of not being able to perform fine detailed editing, while SegVol’s response resolution is low. Fig. 7 shows other slices of the same mouse scan as Fig. 6. The figure shows a good point response on slices even far away from the clicks, illustrating the ability of 3D annotation and reducing annotation effort.

Supported class and zero-shot embedding The supported class and zero-shot segmentation have intrinsic conflicts. For the supported class, the model is prone to overfit to the organ itself and will ignore point clicks. So we have a zero-shot embedding

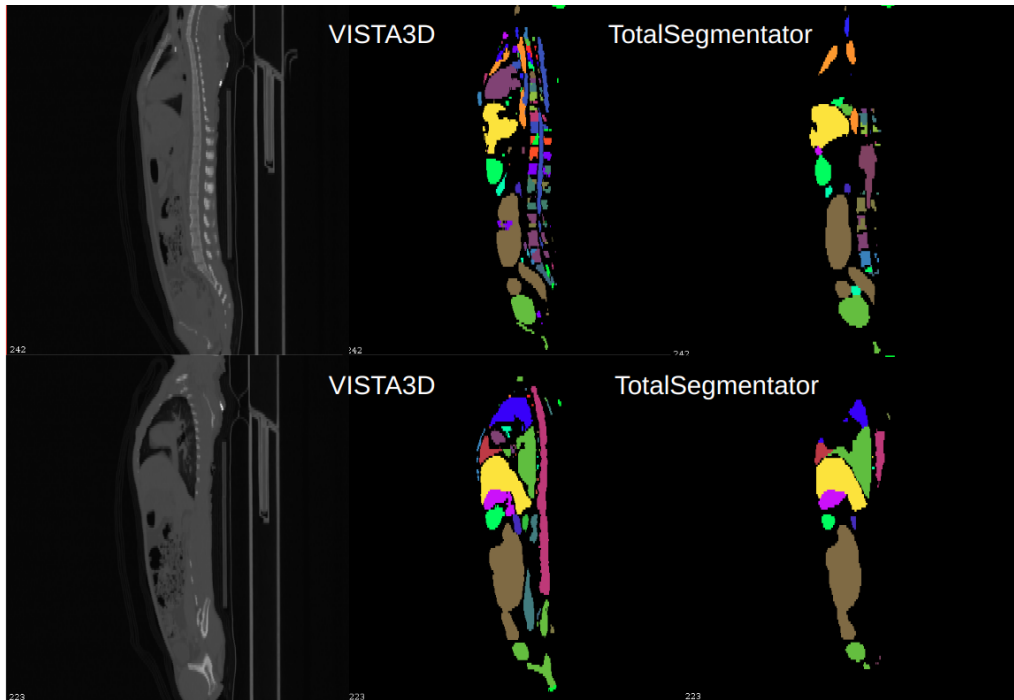


Fig. 2. An example of monkey CT scan (2 sagittal slices). The left figure is the monkey CT image, the middle figure is VISTA3D predictions, and the right figure is from Totalsegmentator. We can see that VISTA3D achieved more robust segmentation.

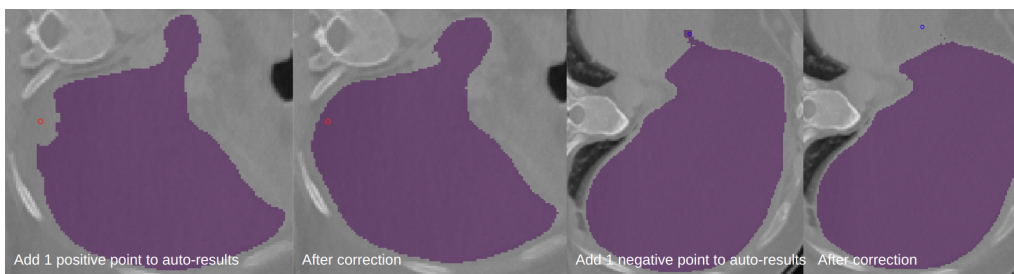


Fig. 3. Correcting automatic segmentation with points. The left figure shows the automatic liver segmentation with a false negative area. After a positive point, the false negative region is corrected. The third figure shows another slice with a false positive and a negative point removed from the region shown in the last figure.

or supported class embedding for the point clicks, which require user input. As shown in Fig. 8, if we want to segment the liver into sub-parts, doing the click in the supported class scheme will require many more points than the zeroshot scheme.

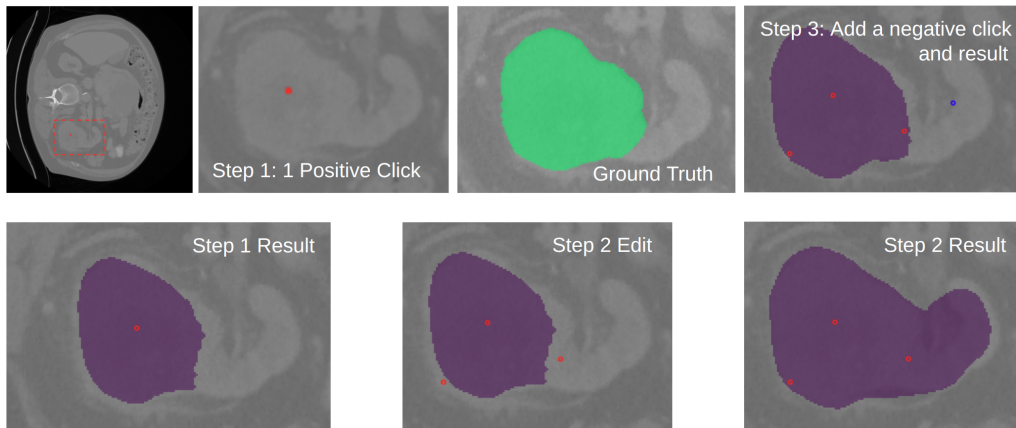


Fig. 4. The zero-shot interactive segmentation on kidney tumor. The first figure shows the region of the tumor. Step 1 click a positive point (red) on the tumor and get the results. Step 2 click more points to refine the details. The result has over-segmentation and add a negative point (blue) on step 3 to get the final results.

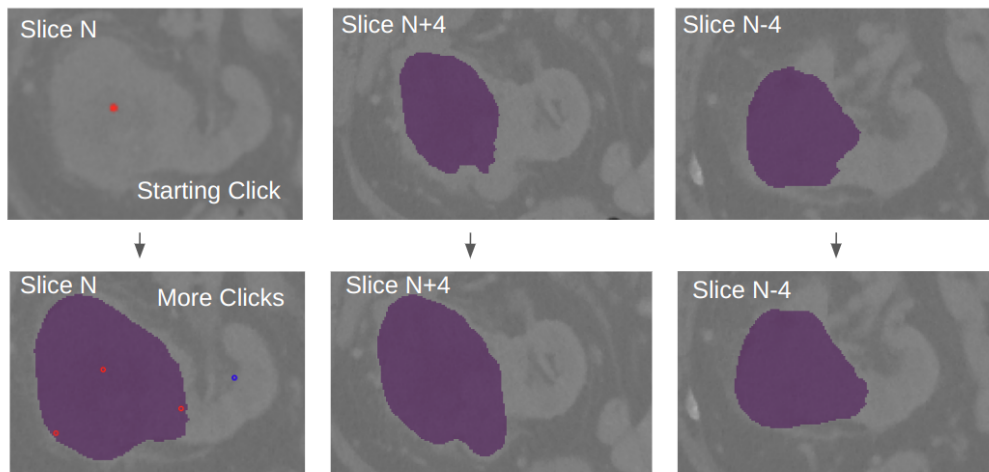


Fig. 5. The adjacent slices (slice N+4 and slice N-4) responses to the clicks on slice N (the same slice and click on Fig. 4). The results show how the clicks affect 3D space.

3.2 Quantitative Results

We provide detailed Dice scores on all the classes of our test datasets. The result is shown in Table. 2

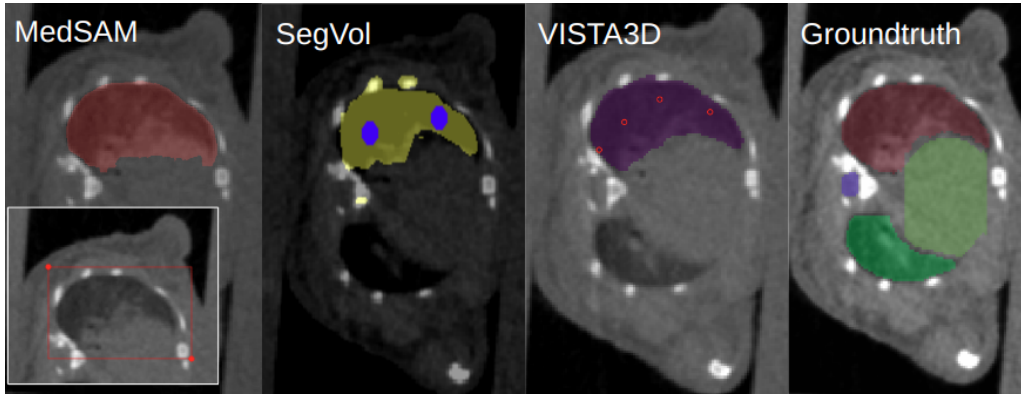


Fig. 6. Interactive segmentation on micro-CT mouse left lung. Baseline results from MedSAM local user interface and SegVol online demo.

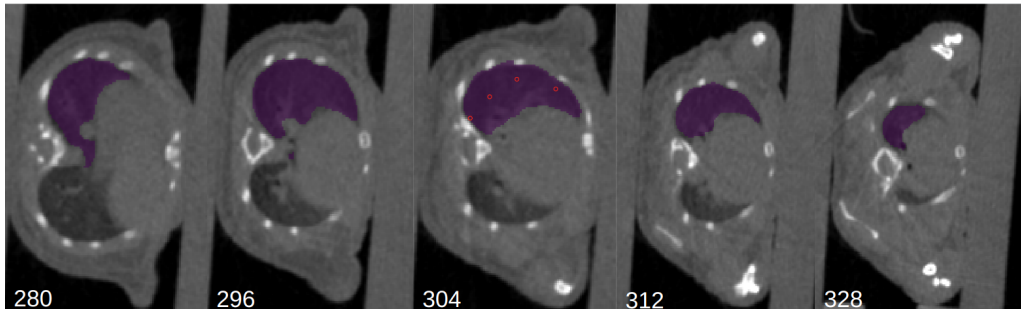


Fig. 7. 3D point response on far away slices. The point click is on slice 304 (same as Fig. 6), but the segmentation on slices 280, 296, 312, and 328 all showed good results, showing the potential of reducing annotation effort in 3D space.

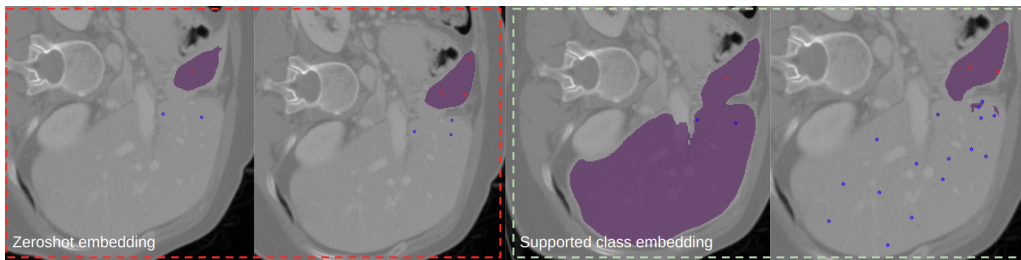


Fig. 8. Use points to forcefully separate liver into substructures. We can see that VISTA3D with zero-shot embedding responds much better to the clicks. However, if the model uses supported class embedding, the model is reluctant to respond to negative points for liver segmentation.

Table 2: Dice score of all the classes on the test datasets.

	Auto-3dSeg	nnUNet	TotalSeg-mentorator	VISTA3D auto	VISTA3D point	VISTA3D auto + point
MSD03 Hepatic Tumor						
liver	0.943	0.947	0.942	0.959	0.874	0.961
hepatic tumor	0.616	0.617	-	0.588	0.701	0.687
MSD06 Lung Tumor						
lung tumor	0.562	0.554	-	0.614	0.682	0.719
MSD07 Pancreatic Tumor						
pancreas	0.785	0.789	0.775	0.819	0.802	0.840
pancreatic tumor	0.485	0.488	-	0.324	0.603	0.638
MSD08 Hepatic Tumor						
hepatic vessel	0.627	0.584	-	0.553	0.582	0.670
hepatic tumor	0.683	0.659	-	0.682	0.733	0.757
MSD09 Spleen						
spleen	0.965	0.967	0.935	0.952	0.938	0.954
MSD10 Colon Tumor						
colon cancer primaries	0.475	0.473	-	0.439	0.609	0.633
AeroPath						
lung	0.982	0.974	0.957	-	-	-
airway	0.896	0.899	-	0.852	0.819	0.867
Bone Lesions						
bone lesions	0.343	0.396	-	0.491	0.536	0.585
BTCV-Abdomen						
spleen	0.954	0.962	0.951	0.944	0.950	0.955
right kidney	0.936	0.951	0.941	0.943	0.937	0.945
left kidney	0.942	0.932	0.944	0.942	0.938	0.946
gallbladder	0.663	0.771	0.739	0.794	0.792	0.807
esophagus	0.740	0.740	0.793	0.779	0.799	0.821
liver	0.964	0.961	0.970	0.967	0.715	0.969
stomach	0.876	0.797	0.946	0.944	0.938	0.946
aorta	0.929	0.909	0.929	0.931	0.925	0.932
inferior vena cava	0.834	0.827	0.854	0.842	0.729	0.856
portal vein and splenic vein	0.649	0.752	0.781	0.775	0.734	0.780
pancreas	0.759	0.820	0.807	0.841	0.797	0.853
right adrenal gland	0.604	0.661	0.696	0.692	0.673	0.699
left adrenal gland	0.638	0.642	0.643	0.646	0.666	0.660
BTCV-Cervix						
bladder	0.730	0.752	0.785	0.800	0.863	0.871
prostate or uterus	0.714	0.675	-	0.587	0.691	0.714
rectum	0.719	0.688	-	-	-	-
small bowel	0.466	0.527	0.437	0.544	0.608	0.679
VerSe						
vertebrae C1	0.795	0.862	0.875	0.859	0.844	0.863
vertebrae C2	0.867	0.852	0.909	0.881	0.862	0.890
vertebrae C3	0.804	0.844	0.882	0.828	0.863	0.869
vertebrae C4	0.796	0.874	0.877	0.857	0.811	0.868
vertebrae C5	0.794	0.855	0.878	0.851	0.861	0.864
vertebrae C6	0.808	0.816	0.877	0.865	0.863	0.874
vertebrae C7	0.798	0.822	0.892	0.857	0.878	0.887

vertebrae T1	0.832	0.800	0.901	0.847	0.898	0.897
vertebrae T2	0.817	0.840	0.887	0.862	0.899	0.905
vertebrae T3	0.808	0.837	0.836	0.848	0.892	0.894
vertebrae T4	0.777	0.775	0.790	0.844	0.896	0.903
vertebrae T5	0.745	0.794	0.776	0.827	0.898	0.908
vertebrae T6	0.713	0.782	0.766	0.818	0.905	0.913
vertebrae T7	0.723	0.887	0.742	0.822	0.912	0.919
vertebrae T8	0.710	0.847	0.759	0.791	0.912	0.920
vertebrae T9	0.722	0.826	0.810	0.804	0.916	0.925
vertebrae T10	0.770	0.852	0.803	0.786	0.922	0.928
vertebrae T11	0.776	0.837	0.820	0.822	0.926	0.932
vertebrae T12	0.835	0.798	0.879	0.870	0.927	0.931
vertebrae L1	0.873	0.871	0.915	0.864	0.930	0.936
vertebrae L2	0.822	0.800	0.871	0.811	0.929	0.932
vertebrae L3	0.787	0.876	0.798	0.752	0.927	0.928
vertebrae L4	0.755	0.773	0.722	0.707	0.930	0.932
vertebrae L5	0.740	0.763	0.716	0.735	0.913	0.919
vertebrae L6	0.434	0.475	-	-	-	-

AbdomenCT-1K

liver	0.978	0.982	0.969	0.974	0.896	0.976
kidney	0.947	0.944	0.912	-	-	-
spleen	0.967	0.976	0.968	0.966	0.959	0.964
pancreas	0.857	0.860	0.828	0.865	0.853	0.881

AMOS22

spleen	0.953	0.946	0.930	0.934	0.933	0.946
right kidney	0.955	0.943	0.940	0.945	0.937	0.949
left kidney	0.944	0.950	0.925	0.931	0.938	0.948
gallbladder	0.779	0.832	0.813	0.847	0.814	0.855
esophagus	0.805	0.808	0.777	0.776	0.783	0.805
liver	0.971	0.972	0.958	0.959	0.901	0.960
stomach	0.858	0.855	0.882	0.876	0.863	0.889
aorta	0.944	0.953	0.914	0.917	0.897	0.921
inferior vena cava	0.889	0.870	0.809	0.855	0.669	0.865
pancreas	0.809	0.840	0.773	0.797	0.757	0.828
right adrenal gland	0.744	0.708	0.683	0.700	0.657	0.721
left adrenal gland	0.740	0.714	0.684	0.704	0.687	0.724
duodenum	0.743	0.754	0.639	0.704	0.337	0.729
bladder	0.824	0.808	0.809	0.826	0.819	0.847
prostate or uterus	0.817	0.827	-	0.788	0.790	0.828

TotalSegmentatorV2

spleen	0.957	0.969	0.982	0.967	0.965	0.971
right kidney	0.949	0.940	0.962	0.934	0.930	0.948
left kidney	0.942	0.922	0.961	0.920	0.921	0.941
gallbladder	0.807	0.843	0.896	0.827	0.782	0.833
liver	0.964	0.965	0.982	0.968	0.944	0.974
stomach	0.929	0.935	0.960	0.931	0.917	0.939
aorta	0.954	0.961	0.961	0.959	0.949	0.965
inferior vena cava	0.892	0.902	0.896	0.883	0.695	0.896
portal vein and splenic vein	0.757	0.830	0.835	0.801	0.744	0.818
pancreas	0.845	0.856	0.917	0.860	0.833	0.877
right adrenal gland	0.805	0.877	0.909	0.863	0.834	0.869

left adrenal gland	0.808	0.866	0.914	0.873	0.851	0.881
left lung upper lobe	0.943	0.939	0.979	0.953	0.931	0.955
left lung lower lobe	0.928	0.953	0.964	0.938	0.899	0.944
right lung upper lobe	0.896	0.912	0.919	0.878	0.872	0.905
right lung middle lobe	0.905	0.939	0.952	0.916	0.909	0.930
right lung lower lobe	0.928	0.950	0.974	0.943	0.893	0.951
vertebrae L5	0.909	0.930	0.946	0.916	0.916	0.933
vertebrae L4	0.899	0.929	0.947	0.899	0.917	0.933
vertebrae L3	0.892	0.927	0.967	0.925	0.934	0.957
vertebrae L2	0.925	0.928	0.975	0.936	0.950	0.968
vertebrae L1	0.904	0.917	0.967	0.919	0.934	0.955
vertebrae T12	0.902	0.912	0.961	0.902	0.930	0.948
vertebrae T11	0.899	0.922	0.970	0.900	0.930	0.952
vertebrae T10	0.900	0.918	0.972	0.901	0.937	0.955
vertebrae T9	0.886	0.918	0.976	0.901	0.936	0.960
vertebrae T8	0.882	0.893	0.967	0.872	0.913	0.949
vertebrae T7	0.822	0.886	0.920	0.831	0.890	0.920
vertebrae T6	0.840	0.902	0.943	0.878	0.910	0.933
vertebrae T5	0.869	0.923	0.944	0.891	0.904	0.930
vertebrae T4	0.876	0.910	0.948	0.887	0.910	0.935
vertebrae T3	0.888	0.926	0.950	0.895	0.903	0.935
vertebrae T2	0.909	0.918	0.967	0.920	0.922	0.949
vertebrae T1	0.907	0.945	0.969	0.933	0.926	0.950
vertebrae C7	0.894	0.943	0.964	0.923	0.901	0.937
vertebrae C6	0.839	0.840	0.941	0.882	0.864	0.917
vertebrae C5	0.797	0.852	0.915	0.825	0.852	0.862
vertebrae C4	0.860	0.859	0.944	0.904	0.881	0.917
vertebrae C3	0.857	0.936	0.956	0.905	0.905	0.926
vertebrae C2	0.908	0.953	0.972	0.910	0.872	0.933
vertebrae C1	0.884	0.862	0.935	0.894	0.848	0.896
esophagus	0.874	0.913	0.952	0.907	0.886	0.916
trachea	0.926	0.945	0.974	0.941	0.910	0.946
brain	0.870	0.946	0.943	0.894	0.892	0.903
left iliac artery	0.822	0.896	0.916	0.895	0.872	0.906
right iliac artery	0.820	0.879	0.915	0.875	0.877	0.899
left iliac vena	0.841	0.898	0.941	0.917	0.899	0.925
right iliac vena	0.834	0.884	0.919	0.890	0.846	0.908
small bowel	0.854	0.868	0.918	0.834	0.840	0.865
duodenum	0.779	0.805	0.900	0.822	0.596	0.848
colon	0.882	0.882	0.948	0.898	0.819	0.906
left rib 1	0.914	0.938	0.948	0.909	0.875	0.918
left rib 2	0.934	0.927	0.966	0.932	0.909	0.943
left rib 3	0.906	0.929	0.950	0.910	0.885	0.907
left rib 4	0.908	0.936	0.947	0.903	0.887	0.927
left rib 5	0.878	0.895	0.933	0.889	0.889	0.928
left rib 6	0.865	0.912	0.925	0.866	0.884	0.916
left rib 7	0.885	0.907	0.942	0.877	0.901	0.934
left rib 8	0.902	0.888	0.955	0.890	0.910	0.941
left rib 9	0.910	0.901	0.953	0.897	0.916	0.944
left rib 10	0.911	0.883	0.949	0.893	0.906	0.937
left rib 11	0.891	0.894	0.949	0.903	0.911	0.938

left rib 12	0.885	0.873	0.912	0.883	0.871	0.909
right rib 1	0.905	0.938	0.945	0.907	0.875	0.912
right rib 2	0.933	0.946	0.959	0.924	0.888	0.929
right rib 3	0.906	0.938	0.931	0.891	0.854	0.900
right rib 4	0.928	0.942	0.949	0.906	0.882	0.926
right rib 5	0.905	0.893	0.916	0.876	0.877	0.914
right rib 6	0.900	0.929	0.951	0.886	0.907	0.932
right rib 7	0.903	0.914	0.960	0.884	0.915	0.942
right rib 8	0.888	0.928	0.959	0.887	0.913	0.941
right rib 9	0.892	0.928	0.950	0.890	0.920	0.946
right rib 10	0.900	0.927	0.949	0.896	0.916	0.945
right rib 11	0.880	0.924	0.933	0.885	0.891	0.924
right rib 12	0.885	0.906	0.917	0.883	0.880	0.907
left humerus	0.911	0.867	0.930	0.854	0.881	0.903
right humerus	0.916	0.794	0.940	0.873	0.884	0.913
left scapula	0.910	0.949	0.959	0.911	0.887	0.921
right scapula	0.916	0.923	0.959	0.922	0.887	0.920
left clavícula	0.955	0.917	0.975	0.952	0.931	0.956
right clavícula	0.937	0.940	0.973	0.945	0.933	0.952
left femur	0.944	0.882	0.970	0.940	0.944	0.954
right femur	0.944	0.911	0.980	0.945	0.957	0.959
left hip	0.944	0.937	0.975	0.947	0.938	0.955
right hip	0.939	0.932	0.986	0.950	0.961	0.959
sacrum	0.925	0.933	0.958	0.915	0.895	0.922
left gluteus maximus	0.925	0.927	0.977	0.940	0.938	0.949
right gluteus maximus	0.917	0.930	0.978	0.937	0.937	0.949
left gluteus medius	0.919	0.926	0.973	0.931	0.923	0.923
right gluteus medius	0.908	0.927	0.978	0.938	0.937	0.946
left gluteus minimus	0.875	0.917	0.965	0.914	0.903	0.919
right gluteus minimus	0.876	0.920	0.967	0.915	0.896	0.921
left autochthon	0.939	0.934	0.978	0.951	0.932	0.953
right autochthon	0.941	0.932	0.976	0.941	0.927	0.947
left iliopsoas	0.876	0.910	0.965	0.921	0.898	0.926
right iliopsoas	0.876	0.916	0.952	0.907	0.898	0.914
bladder	0.890	0.906	0.934	0.899	0.895	0.915
left atrial appendage	0.863	0.900	0.942	0.901	0.873	0.910
brachiocephalic trunk	0.872	0.899	0.936	0.892	0.888	0.915
left brachiocephalic vein	0.881	0.919	0.945	0.903	0.885	0.898
right brachiocephalic vein	0.862	0.909	0.922	0.884	0.869	0.901
left common carotid artery	0.826	0.884	0.925	0.868	0.828	0.891
right common carotid artery	0.755	0.858	0.885	0.811	0.784	0.844
costal cartilages	0.844	0.868	0.888	0.856	0.833	0.864
heart	0.932	0.928	0.937	0.919	0.916	0.924
left kidney cyst	0.623	0.858	0.892	0.618	0.752	0.858
right kidney cyst	0.568	0.841	0.716	0.606	0.615	0.681
prostate	0.743	0.752	0.808	0.744	0.745	0.774
pulmonary vein	0.838	0.820	0.916	0.830	0.847	0.863
skull	0.909	0.849	0.893	0.827	0.769	0.857
spinal cord	0.911	0.950	0.959	0.934	0.905	0.937
sternum	0.896	0.906	0.897	0.899	0.884	0.911
left subclavian artery	0.833	0.901	0.929	0.877	0.857	0.892

right subclavian artery	0.818	0.870	0.916	0.861	0.850	0.885
superior vena cava	0.894	0.899	0.932	0.888	0.905	0.923
thyroid gland	0.832	0.886	0.908	0.866	0.853	0.890
vertebrae S1	0.870	0.906	0.925	0.890	0.880	0.909

4 Additional Discussions

The VISTA3D model design will naturally raise two questions, why not share decoder and why share encoder. If we share the encoder and decoder, then automatic and interactive will be trained together, which will 1) slow down the training. Interactive branch is much more memory intensive than automatic branch, and the supervoxels are only used for interactive training, thus, automatic branch can use a much larger batch size. Combine these two training will reduce automatic branch training iteration and its performance. 2) There are internal conflicts between zero-shot and automatic segmentation, our pilot study showed worse results and our auto-branch is not able to reach state-of-the-art results once trained together with interactive branch. Sharing encoder has two purposes, 1) we support interactive editing over automatic results, the shared encoder could reduce inference computation cost. 2) The interactive branch can be trained with a much broader range of data, thus the encoder can extract more generalizable features and help with the generalizability of automatic segmentation.

References

- Achanta, R., Shaji, A., Smith, K., Lucchi, A., Fua, P., Süsstrunk, S.: SLIC superpixels compared to state-of-the-art superpixel methods. *IEEE transactions on pattern analysis and machine intelligence* **34**(11), 2274–2282 (2012)
- Achiam, J., Adler, S., Agarwal, S., Ahmad, L., Akkaya, I., Aleman, F.L., Almeida, D., Altenschmidt, J., Altman, S., Anadkat, S., et al.: GPT-4 technical report. *arXiv preprint arXiv:2303.08774* (2023)
- et al., A.: The medical segmentation decathlon. *Nature communications* **13**(1), 4128 (2022)
- et al., H.: Artificial intelligence for the detection of COVID-19 pneumonia on chest CT using multinational datasets. *Nature communications* **11**(1), 4080 (2020)
- et al., M.: Abdomenct-1k: Is abdominal organ segmentation a solved problem? *IEEE Transactions on Pattern Analysis and Machine Intelligence* **44**(10), 6695–6714 (2022). <https://doi.org/10.1109/TPAMI.2021.3100536>
- et al., M.: Unleashing the strengths of unlabeled data in pan-cancer abdominal organ quantification: the flare22 challenge. *arXiv preprint arXiv:2308.05862* (2023)
- et al., W.: TotalSegmentator: Robust segmentation of 104 anatomic structures in CT images. *Radiology: Artificial Intelligence* **5**(5), e230024 (2023)
- Armato III, S., McLennan, G., Bidaut, L., McNitt-Gray, M., Meyer, C., Reeves, A., Zhao, B., Aberle, D., Henschke, C., Hoffman, E., et al.: Data from LIDC-IDRI [data set]. *The Cancer Imaging Archive* (2015). <https://doi.org/10.7937/K9/TCIA.2015.L09QL9SX>
- Butoi, V.I., Ortiz, J.J.G., Ma, T., Sabuncu, M.R., Guttag, J., Dalca, A.V.: Universeg: Universal medical image segmentation. In: *Proceedings of the IEEE/CVF International Conference on Computer Vision*. pp. 21438–21451 (2023)
- Cardoso, M.J., Li, W., Brown, R., Ma, N., Kerfoot, E., Wang, Y., Murrey, B., Myronenko, A., Zhao, C., Yang, D., et al.: Monai: An open-source framework for deep learning in healthcare. *arXiv preprint arXiv:2211.02701* (2022)
- Chen, X., Zhao, Z., Zhang, Y., Duan, M., Qi, D., Zhao, H.: Focalclick: Towards practical interactive image segmentation. In: *Proceedings of the IEEE/CVF Conference on Computer Vision and Pattern Recognition*. pp. 1300–1309 (2022)

12. Cheng, J., Ye, J., Deng, Z., Chen, J., Li, T., Wang, H., Su, Y., Huang, Z., Chen, J., Jiang, L., Sun, H., He, J., Zhang, S., Zhu, M., Qiao, Y.: SAM-Med2D (2023)
13. Clark, K., Vendt, B., Smith, K., Freymann, J., Kirby, J., Koppel, P., Moore, S., Phillips, S., Maffitt, D., Pringle, M., et al.: The cancer imaging archive (TCIA): maintaining and operating a public information repository. *Journal of digital imaging* **26**, 1045–1057 (2013)
14. Du, Y., Bai, F., Huang, T., Zhao, B.: Segvol: Universal and interactive volumetric medical image segmentation. *arXiv preprint arXiv:2311.13385* (2023)
15. Hatamizadeh, A., Tang, Y., Nath, V., Yang, D., Myronenko, A., Landman, B., Roth, H.R., Xu, D.: Unetr: Transformers for 3D medical image segmentation. In: *Proceedings of the IEEE/CVF winter conference on applications of computer vision*. pp. 574–584 (2022)
16. He, Y., Nath, V., Yang, D., Tang, Y., Myronenko, A., Xu, D.: SwinUNETR-V2: Stronger swin transformers with stagewise convolutions for 3D medical image segmentation. In: *MICCAI* (2023)
17. He, Y., Yang, D., Roth, H., Zhao, C., Xu, D.: Dints: Differentiable neural network topology search for 3d medical image segmentation. In: *Proceedings of the IEEE/CVF conference on computer vision and pattern recognition*. pp. 5841–5850 (2021)
18. Heller, N., Sathianathen, N., Kalapara, A., Walczak, E., Moore, K., Kaluzniak, H., Rosenberg, J., Blake, P., Rengel, Z., Oestreich, M., et al.: Data from C4KC-KITS [data set]. *The Cancer Imaging Archive* **10** (2019). <https://doi.org/10.7937/TCIA.2019.IX49E8NX>
19. Huang, Y., Yang, X., Liu, L., Zhou, H., Chang, A., Zhou, X., Chen, R., Yu, J., Chen, J., Chen, C., et al.: Segment anything model for medical images? *Medical Image Analysis* **92**, 103061 (2024)
20. Isensee, F., Jaeger, P.F., Kohl, S.A., Petersen, J., Maier-Hein, K.H.: nnU-Net: a self-configuring method for deep learning-based biomedical image segmentation. *Nature Methods* **18**(2), 203–211 (2021)
21. Ji, Y., Bai, H., Yang, J., Ge, C., Zhu, Y., Zhang, R., Li, Z., Zhang, L., Ma, W., Wan, X., et al.: AMOS: A large-scale abdominal multi-organ benchmark for versatile medical image segmentation. *arXiv preprint arXiv:2206.08023* (2022)
22. Ji, Z., Guo, D., Wang, P., Yan, K., Lu, L., Xu, M., Wang, Q., Ge, J., Gao, M., Ye, X., et al.: Continual segment: Towards a single, unified and non-forgetting continual segmentation model of 143 whole-body organs in ct scans. In: *Proceedings of the IEEE/CVF International Conference on Computer Vision*. pp. 21140–21151 (2023)
23. Johnson, C.D., Chen, M.H., Toledano, A.Y., Heiken, J.P., Dachman, A., Kuo, M.D., Menias, C.O., Siewert, B., Cheema, J.I., Obregon, R.G., et al.: Accuracy of CT colonography for detection of large adenomas and cancers. *New England Journal of Medicine* **359**(12), 1207–1217 (2008)
24. Kirillov, A., Mintun, E., Ravi, N., Mao, H., Rolland, C., Gustafson, L., Xiao, T., Whitehead, S., Berg, A.C., Lo, W.Y., et al.: Segment anything. In: *Proceedings of the IEEE/CVF International Conference on Computer Vision*. pp. 4015–4026 (2023)
25. Kolesnikov, A., Dosovitskiy, A., Weissenborn, D., Heigold, G., Uszkoreit, J., Beyer, L., Minderer, M., Dehghani, M., Houtsby, N., Gelly, S., Unterthiner, T., Zhai, X.: An image is worth 16x16 words: Transformers for image recognition at scale. In: *ICLR* (2021)
26. Liu, J., Zhang, Y., Chen, J.N., Xiao, J., Lu, Y., Landman, B., Yuan, Y., Yuille, A., Tang, Y., Zhou, Z.: Clip-driven universal model for organ segmentation and tumor detection. In: *Proceedings of the IEEE/CVF International Conference on Computer Vision*. pp. 21152–21164 (2023)
27. Luo, X., Liao, W., Xiao, J., Chen, J., Song, T., Zhang, X., Li, K., Metaxas, D.N., Wang, G., Zhang, S.: Word: A large scale dataset, benchmark and clinical applicable study for abdominal organ segmentation from ct image. *Medical Image Analysis* **82**, 102642 (Nov 2022)
28. Ma, J., He, Y., Li, F., Han, L., You, C., Wang, B.: Segment anything in medical images. *Nature Communications* **15**, 1–9 (2024)

29. Malimban, J., Lathouwers, D., Qian, H., Verhaegen, F., Wiedemann, J., Brandenburg, S., Staring, M.: Deep learning-based segmentation of the thorax in mouse micro-ct scans. *Scientific reports* **12**(1), 1822 (2022)
30. Moawad, A., Ahmed, A., et al.: Voxel-level segmentation of pathologically-proven adrenocortical carcinoma with Ki-67 expression (Adrenal-ACC-Ki67-Seg)[data set]. *The Cancer Imaging Archive* (2023)
31. Morshid, A., Elsayes, K.M., Khalaf, A.M., Elmohr, M.M., Yu, J., Kaseb, A.O., Hassan, M., Mahvash, A., Wang, Z., Hazle, J.D., et al.: A machine learning model to predict hepatocellular carcinoma response to transcatheter arterial chemoembolization. *Radiology: Artificial Intelligence* **1**(5), e180021 (2019)
32. Myronenko, A.: 3D MRI brain tumor segmentation using autoencoder regularization. In: *MICCAI Brainles. Brain Tumor Segmentation (BraTS) Challenge*. pp. 311–320. Springer (2018)
33. Myronenko, A., Yang, D., He, Y., Xu, D.: Aorta segmentation from 3D CT in MICCAI SEG.A. 2023 challenge. In: *MICCAI 2023. 3D Segmentation of the Aorta Challenge* (2023)
34. Myronenko, A., Yang, D., He, Y., Xu, D.: Auto3DSeg for brain tumor segmentation from 3D MRI in BraTS 2023 challenge. In: *MICCAI. Brain Tumor Segmentation (BraTS) Challenge*. (2023)
35. Myronenko, A., Yang, D., He, Y., Xu, D.: Automated 3D segmentation of kidneys and tumors in MICCAI KiTS 2023 challenge. In: *MICCAI 2023. International Challenge on Kidney and Kidney Tumor Segmentation*. pp. 1–7. Springer (2023)
36. Rister, B., Yi, D., Shivakumar, K., Nobashi, T., Rubin, D.L.: CT-ORG, a new dataset for multiple organ segmentation in computed tomography. *Scientific Data* **7**(1), 381 (2020)
37. Roth, H., Farag, A., Turkbey, E., Lu, L., Liu, J., Summers, R.: Data from pancreas-CT (version 2)[data set]. *The Cancer Imaging Archive* (2016). <https://doi.org/10.7937/K9/TCIA.2016.tNB1kqBU>
38. Roth, H.R., Lu, L., Farag, A., Shin, H.C., Liu, J., Turkbey, E.B., Summers, R.M.: Deeporgan: Multi-level deep convolutional networks for automated pancreas segmentation. In: *MICCAI*. pp. 556–564. Springer (2015)
39. Saltz, J., Saltz, M., Prasanna, P., Moffitt, R., Hajagos, J., Bremer, E., Balsamo, J., Kurc, T.: Stony Brook university COVID-19 positive cases. *the cancer imaging archive* **4** (2021). <https://doi.org/10.7937/TCIA.BBAG-2923>
40. Sekuboyina, A., Husseini, M.E., Bayat, A., Löffler, M., Liebl, H., Li, H., Tetteh, G., Kukačka, J., Payer, C., Štern, D., et al.: Verse: A vertebrae labelling and segmentation benchmark for multi-detector CT images. *Medical image analysis* **73**, 102166 (2021)
41. Shen, L., Shang, F., Yang, Y., Huang, X., Xiang, S.: Segicl: A universal in-context learning framework for enhanced segmentation in medical imaging. *arXiv preprint arXiv:2403.16578* (2024)
42. Simpson, A.L., Peoples, J., Creasy, J.M., Fichtinger, G., Gangai, N., Keshavamurthy, K.N., Lasso, A., Shia, J., D’Angelica, M.I., Do, R.K.: Preoperative CT and survival data for patients undergoing resection of colorectal liver metastases. *Scientific Data* **11**(1), 172 (2024)
43. Støverud, K.H., Bouget, D., Pedersen, A., Leira, H.O., Langø, T., Hofstad, E.F.: AeroPath: An airway segmentation benchmark dataset with challenging pathology. *arXiv preprint arXiv:2311.01138* (2023)
44. Tang, Y., Yang, D., Li, W., Roth, H.R., Landman, B., Xu, D., Nath, V., Hatamizadeh, A.: Self-supervised pre-training of swin transformers for 3D medical image analysis. In: *Proceedings of the IEEE/CVF conference on computer vision and pattern recognition*. pp. 20730–20740 (2022)
45. Team, G., Anil, R., Borgeaud, S., Wu, Y., Alayrac, J.B., Yu, J., Soricut, R., Schalkwyk, J., Dai, A.M., Hauth, A., et al.: Gemini: a family of highly capable multimodal models. *arXiv preprint arXiv:2312.11805* (2023)

46. Team, N.L.S.T.R.: Reduced lung-cancer mortality with low-dose computed tomographic screening. *New England Journal of Medicine* **365**(5), 395–409 (2011)
47. Touvron, H., Martin, L., Stone, K., Albert, P., Almahairi, A., Babaei, Y., Bashlykov, N., Batra, S., Bhargava, P., Bhosale, S., et al.: Llama 2: Open foundation and fine-tuned chat models. arXiv preprint arXiv:2307.09288 (2023)
48. Ulrich, C., Isensee, F., Wald, T., Zenk, M., Baumgartner, M., Maier-Hein, K.H.: Multi-dataset approach to medical image segmentation: Multitalent. In: *BVM Workshop*. pp. 78–78. Springer (2024)
49. Wang, H., Guo, S., Ye, J., Deng, Z., Cheng, J., Li, T., Chen, J., Su, Y., Huang, Z., Shen, Y., Fu, B., Zhang, S., He, J., Qiao, Y.: Sam-med3d (2023)
50. Wu, J., Fu, R., Fang, H., Liu, Y., Wang, Z., Xu, Y., Jin, Y., Arbel, T.: Medical SAM adapter: Adapting segment anything model for medical image segmentation. arXiv preprint arXiv:2304.12620 (2023)
51. Zhao, Z., Zhang, Y., Wu, C., Zhang, X., Zhang, Y., Wang, Y., Xie, W.: One model to rule them all: Towards universal segmentation for medical images with text prompts. arXiv preprint arXiv:2312.17183 (2023)